Editors' Suggestion

Chip-Scale Packages for a Tunable Wavelength Reference and Laser Cooling Platform

S. Dyer,[1] K. Gallacher,[2] U. Hawley,[2] A. Bregazzi,[1] P.F. Griffin,[1] A.S. Arnold,[1] D.J. Paul,[2] E. Riis,[1] and J.P. McGilligan[1,*]

[1] *SUPA and Department of Physics, University of Strathclyde, Glasgow G4 0NG, United Kingdom*

[2] *James Watt School of Engineering, University of Glasgow, Rankine Building, Oakfield Avenue, Glasgow G12 8LT, United Kingdom*

(Received 7 December 2022; revised 17 February 2023; accepted 27 February 2023; published 5 April 2023)

We demonstrate a tunable, chip-scale wavelength reference to greatly reduce the complexity and volume of cold-atom sensors. A 1-mm optical path length microfabricated cell provides an atomic wavelength reference, with dynamic frequency control enabled by Zeeman-shifting the atomic transition through the magnetic field generated by the printed-circuit-board coils. The dynamic range of the laser frequency stabilization system is evaluated and used in conjunction with an improved generation of chip-scale cold-atom platforms that traps 4 million ^{87}Rb atoms. The scalability and component consolidation provide a key step forward in the miniaturization of cold-atom sensors.

DOI: 10.1103/PhysRevApplied.19.044015

I. INTRODUCTION

The miniaturization of cold-atom platforms for remote sensing and portability has tantalizing prospects for next-generation quantum technology [1–5]. Owing to the long interrogation times achievable with laser cooling, the development of on-chip cold-atom platforms could improve the stability of current thermal atomic sensors to the benefit of applications in navigation, geological surveying, communication, and precision timing, driving towards fully integrated atomic systems.

Recent research has demonstrated drastic improvements in the scalability of critical components at the heart of atomic sensors. While initially focused on the scalability of thermal atom packages, the microfabrication of core components revolutionized the scalability in a plethora of instruments, including atomic clocks [6–8], magnetometers [9–11], and wavelength references [12,13]. At the heart of many of these devices is a microelectromechanical systems (MEMS) vapor cell. Typically formed from a glass-silicon-glass wafer stack, the on-chip thermal vapor system offers a simplicity and design versatility that complements its application in precision spectroscopy [14–17].

The miniaturization of thermal atom packages has also driven forward the scalability of cold-atom sensors. Recent studies have demonstrated cold-atom sensor scalability through the coupling of photonic integrated circuits [18–20], metasurfaces [21,22], diffractive optics [23–25], planar coil systems [26], and microfabricated alkali sources [27,28]. More recently, MEMS vapor cells capable of sustaining an ultrahigh vacuum (UHV) have been shown in conjunction with microfabricated grating chips as an on-chip platform for cold atoms [29]. Parallel avenues of research have aimed to address the miniaturization and simplicity of cold-atom systems through the development of plug-and-play interfaces, making use of conventional off-the-shelf optics [30,31]. Many of these cold-atom systems, however, have focused on individual component development, such that a fully integrated cold-atom platform has remained elusive.

In this Article, we demonstrate a tunable wavelength reference at 780 nm that is coupled with a chip-scale laser cooling platform for Rb atoms. A single optical package enables laser frequency tuning and stabilization in a microfabricated vapor cell, sandwiched between a printed-circuit-board (PCB) coil pair. The dynamic range of the chip-scale package is evaluated as a viable replacement to standard larger components used for real-time frequency control, such as acousto-optical modulators. The wavelength reference is paired with a chip-scale cold-atom platform to demonstrate device simplicity and compatibility for laser-cooling applications. Finally, the combined apparatus demonstrates laser cooled atom numbers greater than 10^6 in thick silicon MEMS vacuum cells. The union of such components provides a key step in the scalability and mass production of cold-atom systems.

*james.mcgilligan@strath.ac.uk

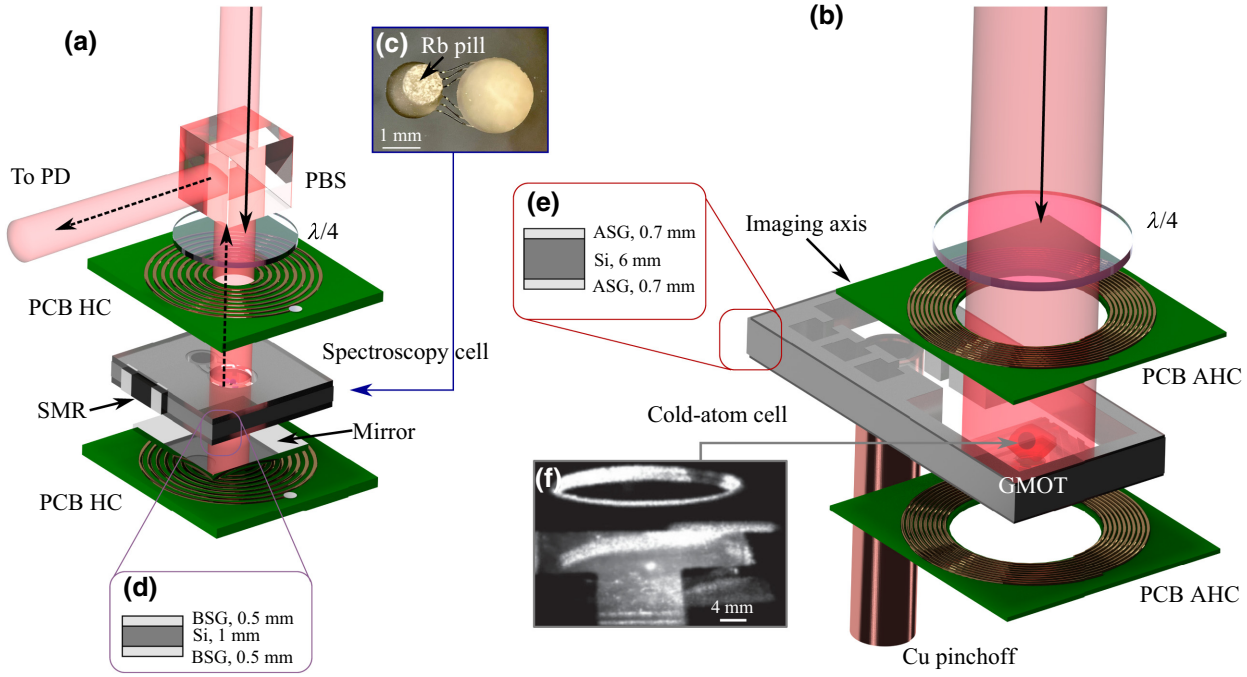

FIG. 1. A schematic diagram overview of the chip-scale wavelength and cooling platforms. (a) A MEMS cell-based wavelength reference using saturated absorption spectroscopy. Solid/dashed lines indicates the incident/retro-reflected beam. PD: photodiode. PCB HC: printed-circuit-board Helmholtz coils. PBS: polarizing beam splitter. SMR: surface-mounted resistor. (b) MEMS cell GMOT incorporated laser cooling platform with planar coils. GMOT: grating magneto-optical trap. PCB AHC: printed-circuit-board anti-Helmholtz coils. (c) Microscope image of the MEMS cell in the wavelength reference package. (d) Layer structure for the wavelength reference MEMS cell stack. BSG: borosilicate glass. (e) Layer structure for the UHV-MEMS cell stack. ASG: aluminosilicate glass. (f) Example image of the cold-atom sample formed from the combined chip-scale platforms.

II. EXPERIMENTAL SETUP

The experimental apparatus used for the wavelength reference and chip-scale laser cooling platform is shown in Figs. 1(a) and 1(b), respectively. The light source is provided from a butterfly- packaged volume-Bragg reflector (VBR) laser centered at 780 nm. The light from the VBR is incident through a 5-mm polarizing beam splitter (PBS), with one arm coupled into our chip-scale wavelength reference.

To enable miniaturization, the bulky optical and electronic system required for an acoustic optical modulator (AOM) was replaced with the tunable Zeeman lock [32]. The laser wavelength reference is provided by saturated absorption spectroscopy through a MEMS cell, shown at the center of Fig. 1(a). The MEMS spectroscopy cell, shown in Fig. 1(c), is composed of a 1-mm- thick silicon frame anodically bonded at both interfaces to 0.5-mm-thick borosilicate glass wafers, as highlighted in Fig. 1(d). The silicon frame is deep- reactive-ion-etched using an anisotropic Bosch process [33] to form a two-chamber cell connected via 650-μm-wide, non-line-of-sight channels. The first chamber houses a micropill-based alkali vapor source (SAES Rb/AMAX/Pill1-0.6). The second chamber acts as the spectroscopy region with a 2-mm-diameter aperture. The cell is mechanically diced to dimensions of $10 \times 10 \times 2$ mm and a surface-mounted resistor is adhered to the side of the silicon frame to provide heating. Prior to the implementation of the spectroscopy cell in the apparatus, the pill is laser-activated with 1 W of 1070-nm laser light focused onto the pill surface for 10 s [34].

The spectroscopy cell is sandwiched between a pair of PCB Helmholtz coils. Each 1-mm-thick PCB is double-side-printed and electrically connected via a circuit through-hole to increase the number of turns over the given board volume. The coil is formed of 35-μm-thick copper layer wires with 170-μm-width deposited on the surfaces of the board to form a total of 14 turns, with a mean radius of 3.3 mm ($R_{\text{min}} = 2.2$ mm, $R_{\text{max}} = 4.5$ mm). The center of the coil has a 1.5 mm radius aperture that is aligned for optical interrogation of the spectroscopy cell. The coils and cell are held firmly in place within a three-dimensional printed mount, formed from high-temperature plastic that ensures robust alignment through a press-fit and glue. The laser is frequency modulated at 250 kHz via current dithering. The output from the laser is passed through a PBS, circularly polarized with a $\lambda/4$ wave plate before the spectroscopy cell and reflected by a dielectric reflector, mounted to the back of the MEMS cell. The output transmission from the spectroscopy system is directed through the PBS to a photodiode, where

the absorption signal is passed to external electronics for demodulation, and the resulting error signal is used to electronically feed back to the VBR current for frequency stabilization.

The laser is locked directly to the $F = 2 \rightarrow F' = 3$ cooling transition, and a frequency offset is provided from the PCB Helmholtz coils, with the magnetic field orientation illustrated in Fig. 2(a). The magnetic field is simulated from a numerical solution to the Biot-Savart law, for parameters meeting that of the PCB. The offset mechanism uses a bias magnetic field along the axis of the beam, which induces a shift to the Zeeman sublevels. Circularly polarized light is used to optically pump the atoms into the stretched states. As such, the magnetically sensitive sub-Doppler features can be exploited to tune the laser lock frequency while avoiding the optical losses typical of a double-passed AOM setup [35]. To determine the versatility of the frequency offset, a beat note was measured against an external-cavity diode laser (ECDL), which was stabilized to the $F = 2 \rightarrow F' = 2, 3$ crossover transition of ^{87}Rb using saturated absorption spectroscopy on a separate reference cell. The beat-note signal was obtained by overlapping light from each laser onto a fast photodiode and the output frequency was tracked on a frequency counter.

The second light arm from the VBR that is not incident on the wavelength reference is passed through a free-space electro-optical modulator (EOM) driven at 6.58 GHz to generate 5% sidebands for hyperfine repumping in the laser cooling process. The light is then fiber-coupled and expanded in free space to the cold-atom system. The light is circularly polarized with a $\lambda/4$ wave plate before being incident through the UHV-MEMS cold-atom cell. The cold-atom cell, shown in Fig. 1(b), is composed of a 6-mm-thick silicon frame, fabricated with water-jet processing to achieve the deep silicon cut [36]. The silicon wafer is anodically bonded at the upper and lower surfaces to 700-μm-thick aluminosilicate glass wafers, as highlighted in Fig. 1(e). Unlike the spectroscopy cell, aluminosilicate glass is elected for the cold-atom cell due to the favorable helium permeation rates that would be expected to improve the vacuum longevity relative to borosilicates [37].

The upper glass wafer is connected to an ion pump and resistively heated alkali dispenser through a copper pinchoff tube adhered over a mechanically drilled glass through-hole. The cold-atom cell outer dimensions are $70 \times 34 \times 7.4$ mm with a $20 \times 20 \times 6$ mm laser cooling region, which accommodates the surface area of the grating chip. The three-segment grating chip is fabricated with a 1100 nm period over the 2×2 cm surface area of the chip. At the center of the grating, a 2-mm-diameter hole has been laser cut for optical access and imaging [38]. The grating chip is placed immediately below the cold-atom cell lower window to ensure a maximum optical overlap volume exists within the cold-atom cell vacuum volume. In previous work, absorption imaging through

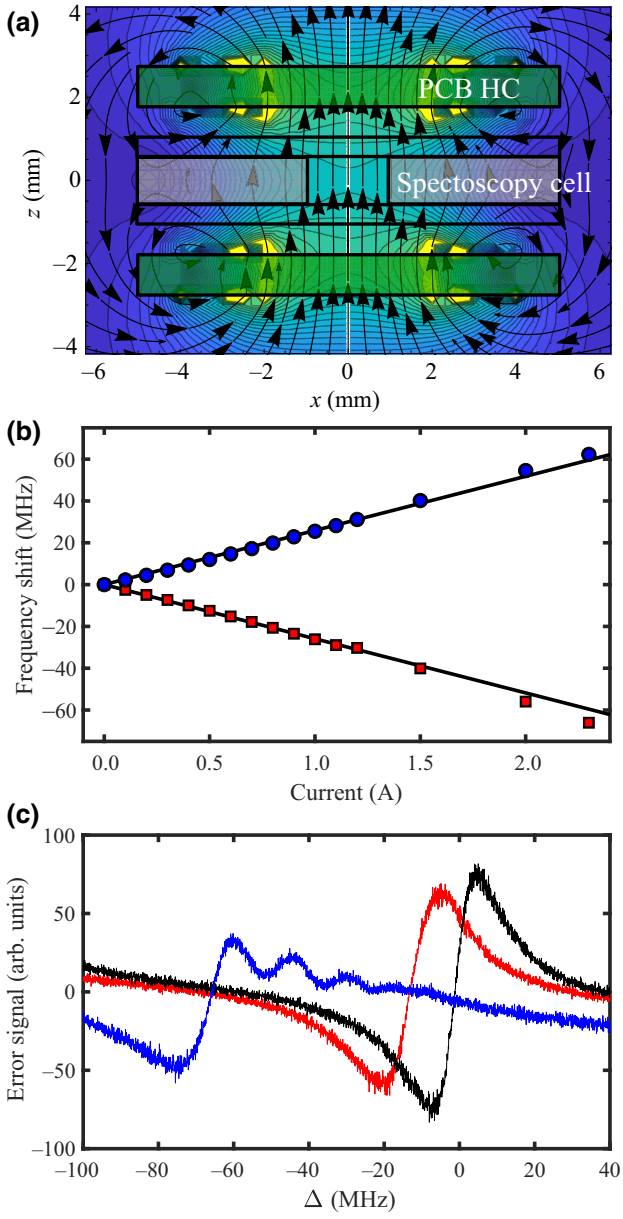

FIG. 2. (a) Printed-circuit-board generated Helmholtz magnetic field orientation through the MEMS spectroscopy cell. (b) Measured frequency shift as a function of the coil current, where blue circles (red squares) represent a positive (negative) applied magnetic field magnitude. The black lines highlight a ±1.4 MHz/G frequency shift. (c) The Zeeman-shifted error signal measured with a single shot at 12 MHz detuning (red), on resonance (black) and at 66 MHz detuning (blue).

the grating chip was required to overcome surface scatter and resolve the trapped atom number. However, this approach was not suited to the current apparatus due to the removal of an AOM, previously used for intensity control in the imaging light sequence. Instead, this generation of the cold-atom cell was fabricated with a $30 \times 8 \times 6$ mm channel leading from the pinchoff region to the cooling

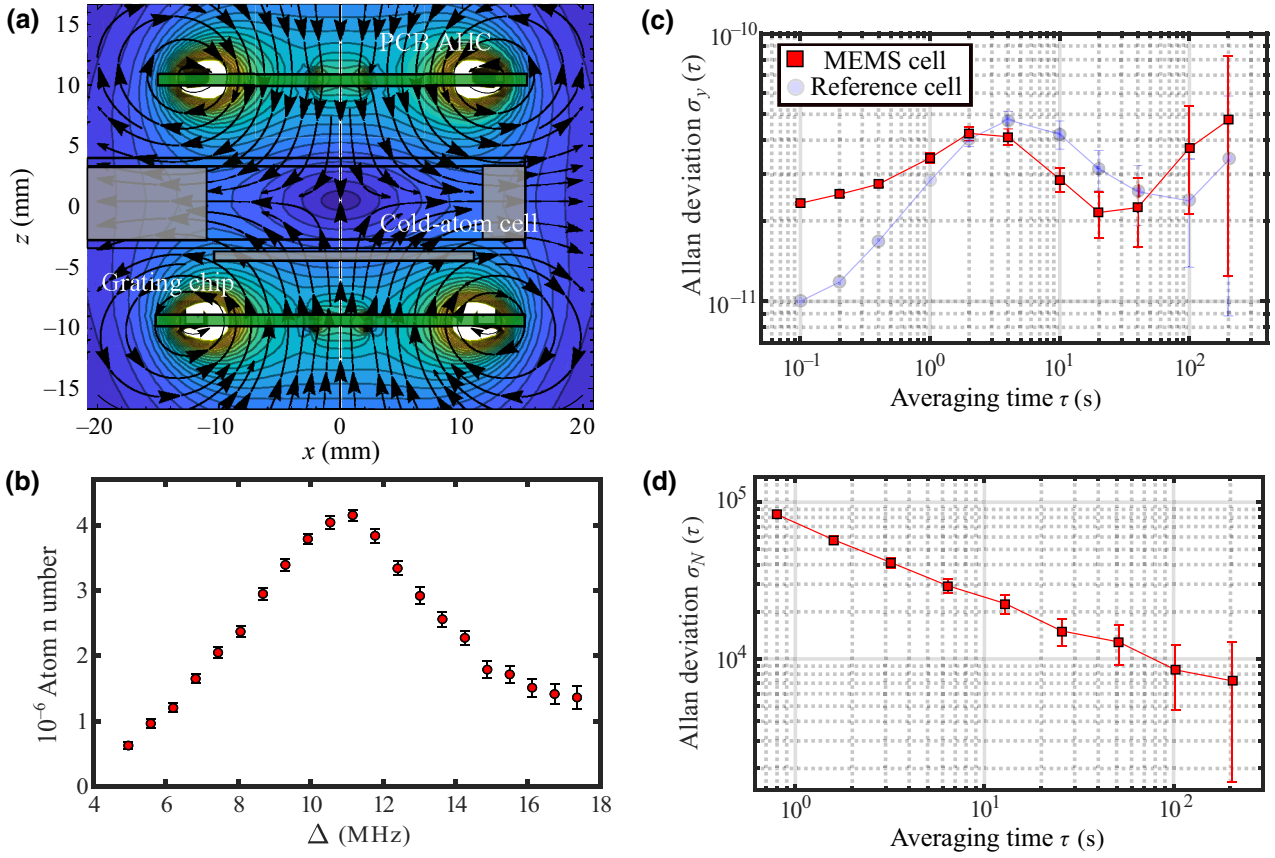

FIG. 3. (a) Printed-circuit-board-generated anti-Helmholtz magnetic field orientation through the 6-mm-thick cold-atom cell. (b) Measured atom number as a function of laser lock frequency, provided by the MEMS wavelength reference. (c) Overlapping Allan deviation of the beat-note signal when the VBR laser is stabilized to the tunable wavelength reference and a 7-cm reference cell, shown in red squares and blue circles, respectively. (d) Simultaneously measured atom number stability from the cold-atom platform.

region to enable fluorescence imaging of the cold atoms by allowing a low angular displacement between the cell and imaging system. The low incident angle for imaging avoids diffracted orders from the grating chip and greatly reduces the surface scatter from the cell walls, glass, and grating. An example of this imaging axis is shown in Fig. 1(f). The cold-atom cell and grating are sandwiched by a PCB anti-Helmholtz coil (PCB AHC). These PCB coils are of the same thickness and wire properties as the previously described Helmholtz PCBs. Each PCB AHC, however, is formed of 30 turns, 15 on each side, with a mean radius of 12.5 mm ($R_{\text{min}} = 10.2$ mm, $R_{\text{max}} = 14.9$ mm).

III. RESULTS

The induced frequency shift for weak magnetic fields, shown in Fig. 2(b), was found to be 1.42 ± 0.12 MHz/G. This value is in agreement with the expected shift for the $F = 2, m_F = 2 \rightarrow F' = 3, m_F = 3$ transition, indicating stretched-state optical pumping. However, the demonstrated ± 60 MHz detuning range is sufficient to achieve a red-detuned lock for the magneto-optical trap, where the trapped atom number is typically optimum in Rb for a detuning between $\Delta = -\Gamma$ and $\Delta = -2\Gamma$, where Γ is the natural linewidth of the excited state ($\Gamma_{D_2} = 2\pi \times 6.1$ MHz) [39]. Over this detuning range, the PCB HC coil pair require less than 0.7 W of electrical power. The error signal from the spectroscopy cell, shown for $\Delta = 12$ MHz in Fig. 2(c) with a red line, has no significant amplitude or linewidth degradation compared to the resonant signal, shown in black. However, for stronger magnetic fields, the amplitude of the error signal is degraded as the magnetic field lifts the degeneracy of the Zeeman sublevels, as can be seen with the blue line at a detuning of $\Delta = 66$ MHz. The detuning range here could also prove beneficial to the frequency detunings typical of optical molasses [4].

To demonstrate the applicability of the wavelength reference to cold-atom sensors, the VBR was locked to the cooling transition, and coupled into the chip-scale cold-atom platform. To aid further miniaturization, traditionally large wire-wound anti-Helmholtz coils have been replaced in favor of a PCB solution. Each double-sided PCB AHC used in the cold-atom system has a resistance of 10 Ω and draws 1 A of current to achieve 20 G/cm, with the field

orientation relative to the other system components shown in Fig. 3(a).

The increased vacuum cell volume of the cold-atom cell, compared to previous work [29,38], has been made possible from the recently demonstrated water-jet cutting of silicon wafers [36]. The improved cell volume now enables approximately 93% of the grating magneto-optical trap (GMOT) optical overlap volume to coincide within the cold-atom cell [38]. Due to this, an optimum atom number of 4×10^6 is obtained in the chip-scale platform for a detuning of 11 MHz, as demonstrated in Fig. 3(b), agreeing with previous GMOT work [23]. It was observed that with an incident intensity of approximately 13 mW/cm^2, the atom number would reach a maximum at 20 G/cm.

Finally, the frequency fluctuations of the chip-scale wavelength reference were temporally measured, with the impact on the measured atom number from the cold-atom platform simultaneously tracked. The frequency fluctuations were tracked from a beat note measured against a separate ECDL, as described in Sec. II. During this measurement the detuning was set to 12 MHz, which produced an atom number of about 3×10^6. The relative stability of the wavelength reference is illustrated in Fig. 3(c). The observed relative frequency stability is of the order of 10^{-11} for all integration windows. While this stability does not meet the performance of state-of-the-art on-chip wavelength reference [12], it is suitable for keeping the laser drift well below the 6-MHz linewidth of the cooling transition to satisfy the miniaturization of the cold-atom apparatus. Furthermore, when the tunable wavelength reference is replaced with a 7-cm reference cell, a similar stability was observed, as demonstrated in Fig. 3(c), indicating that the stability is not limited by the MEMS package. The simultaneously measured atom number stability, shown in Fig. 3(d), integrates down with a slope of $\tau^{-1/2}$, demonstrating that the frequency fluctuations of the wavelength reference have no contribution to the stability of the trapped atom number.

The amalgamation of these on-chip technologies has successfully demonstrated a significant scalability in cold-atom technology, while offering a simplified optical system comprised of planar components.

IV. CONCLUSION

We have demonstrated an on-chip solution for wavelength referencing in cold-atom systems. The simple architecture and mass-producible components are suitable for implementation in a wide range of quantum technologies, with a detuning range exceeding ±60 MHz demonstrated in constant use, and increased values possible for short time intervals. The amalgamation with the 6-mm-thick silicon based UHV-MEMS cell directly demonstrates the applicability of the tunable wavelength reference as a suitable replacement for traditionally bulky cold-atom optical systems.

ACKNOWLEDGMENTS

The authors would like to thank R. Boudot for useful conversations and M. Mrozowski for help with PCB fabrication. The authors acknowledge funding from Defence Security and Technology Laboratory, Engineering and Physical Sciences Research Council (EP/T001046/1), and Defence and Security Accelerator. The authors would like to acknowledge support from the INMAQS collaboration (EP/W026929/1). J.P.M. gratefully acknowledges funding from a Royal Academy of Engineering Research Fellowship and D.J.P. from a Royal Academy of Engineering Research Chair in Emerging Technologies (CiET2021\123). A.B. was supported by a PhD studentship from the Defence Science and Technology Laboratory (Dstl).

[1] M. Takamoto, I. Ushijima, N. Ohmae, T. Yahagi, K. Kokado, H. Shinkai, and H. Katori, Test of general relativity by a pair of transportable optical lattice clocks, Nat. Photonics **14**, 411 (2020).

[2] Y. Bidel, O. Carraz, R. Charrière, M. Cadoret, N. Zahzam, and A. Bresson, Compact cold atom gravimeter for field applications, Appl. Phys. Lett. **102**, 144107 (2013).

[3] B. Stray, *et al.*, Quantum sensing for gravity cartography, Nature **602**, 590 (2022).

[4] J. P. McGilligan, K. Gallacher, P. F. Griffin, D. J. Paul, A. S. Arnold, and E. Riis, Micro-fabricated components for cold atom sensors, Rev. Sci. Instrum. **93**, 091101 (2022).

[5] X. H. Bao, A. Reingruber, P. Dietrich, J. Rui, A. Dück, T. Strassel, L. Li, N. L. Liu, B. Zhao, and J. W. Pan, Efficient and long-lived quantum memory with cold atoms inside a ring cavity, Nat. Phys. **8**, 517 (2012).

[6] Z. L. Newman, V. Maurice, C. Fredrick, T. Fortier, H. Leopardi, L. Hollberg, S. A. Diddams, J. Kitching, and M. T. Hummon, High-performance, compact optical standard, Opt. Lett. **46**, 4702 (2021).

[7] S. Knappe, V. Shah, P. D. D. Schwindt, L. Hollberg, J. Kitching, L.-A. Liew, and J. Moreland, A microfabricated atomic clock, Appl. Phys. Lett. **85**, 1460 (2004).

[8] M. Hasegawa, R. Chutani, C. Gorecki, R. Boudot, P. Dziuban, V. Giordano, S. Clatot, and L. Mauri, Microfabrication of cesium vapor cells with buffer gas for MEMS atomic clocks, Sens. Actuators, A **167**, 594 (2011).

[9] P. D. D. Schwindt, B. Lindseth, S. Knappe, V. Shah, J. Kitching, and L.-A. Liew, Chip-scale atomic magnetometer with improved sensitivity by use of the M_x technique, Appl. Phys. Lett. **90**, 081102 (2007).

[10] M. C. D. Tayler, K. Mouloudakis, R. Zetter, D. Hunter, V. G. Lucivero, S. Bodenstedt, L. Parkkonen, and M. W. Mitchell, Miniature Biplanar Coils for Alkali-Metal-Vapor Magnetometry, Phys. Rev. Appl. **18**, 014036 (2022).

[11] D. Hunter, T. E. Dyer, and E. Riis, Accurate optically pumped magnetometer based on Ramsey-style interrogation, Opt. Lett. **47**, 1230 (2022).
[12] M. T. Hummon, S. Kang, D. G. Bopp, Q. Li, D. A. Westly, S. Kim, C. Fredrick, S. A. Diddams, K. Srinivasan, V. Aksyuk, and J. E. Kitching, Photonic chip for laser stabilization to an atomic vapor with 10^{11} instability, Optica **5**, 443 (2018).
[13] J. Kitching, Chip-scale atomic devices, Appl. Phys. Rev. **5**, 031302 (2018).
[14] L.-A. Liew, S. Knappe, J. Moreland, H. Robinson, L. Hollberg, and J. Kitching, Microfabricated alkali atom vapor cells, Appl. Phys. Lett. **84**, 2694 (2004).
[15] Y. Pétremand, C. Affolderbach, R. Straessle, M. Pellaton, D. Briand, G. Mileti, and N. F. de Rooij, Microfabricated rubidium vapour cell with a thick glass core for small-scale atomic clock applications, J. Micromech. Microeng. **22**, 025013 (2012).
[16] R. Chutani, V. Maurice, N. Passilly, C. Gorecki, R. Boudot, M. Abdel Hafiz, P. Abbé, S. Galliou, J.-Y. Rauch, and E. de Clercq, Laser light routing in an elongated micromachined vapor cell with diffraction gratings for atomic clock applications, Sci. Rep. **5**, 14001 (2015).
[17] S. Karlen, J. Haesler, T. Overstolz, G. Bergonzi, and S. Lecomte, Sealing of MEMS atomic vapor cells using Cu-Cu thermocompression bonding, J. Microelectromech. Syst. **29**, 95 (2020).
[18] W. R. McGehee, W. Zhu, D. S. Barker, D. Westly, A. Yulaev, N. Klimov, A. Agrawal, S. Eckel, V. Aksyuk, and J. J. McClelland, Magneto-optical trapping using planar optics, New J. Phys. **23**, 013021 (2021).
[19] N. Chauhan, D. Bose, M. Puckett, R. Moreira, K. Nelson, and D. J. Blumenthal, in *Conference on Lasers and Electro-Optics (2019)* (Optical Society of America, 2019).
[20] A. Isichenko, N. Chauhan, D. Bose, P. D. Kunz, and D. J. Blumenthal, in *Optical Sensors and Sensing Congress (2022)* (Optical Society of America, 2022).
[21] A. Yulaev, W. Zhu, C. Ropp, D. A. Westly, G. Simelgor, C. Zhang, H. J. Lezec, A. Agrawal, and V. A. Aksyuk, in *Optical Fiber Communication Conference (OFC) 2021* (Optica Publishing Group, 2021), p. F2B.1.
[22] L. Zhu, X. Liu, B. Sain, M. Wang, C. Schlickriede, Y. Tang, J. Deng, K. Li, J. Yang, M. Holynski, S. Zhang, T. Zentgraf, K. Bongs, Y.-H. Lien, and G. Li, A dielectric metasurface optical chip for the generation of cold atoms, Sci. Adv. **6**, eabb6667 (2020).
[23] C. C. Nshii, M. Vangeleyn, J. P. Cotter, P. F. Griffin, E. A. Hinds, C. N. Ironside, P. See, A. G. Sinclair, E. Riis, and A. S. Arnold, A surface-patterned chip as a strong source of ultracold atoms for quantum technologies, Nat. Nanotechnol. **8**, 321 (2013).
[24] V. A. Henderson, M. Y. H. Johnson, Y. B. Kale, P. F. Griffin, E. Riis, and A. S. Arnold, Optical characterisation of microfabricated fresnel zone plates for atomic waveguides, Opt. Express **28**, 9072 (2020).
[25] J. P. McGilligan, P. F. Griffin, R. Elvin, S. J. Ingleby, E. Riis, and A. S. Arnold, Grating chips for quantum technologies, Sci. Rep. **7**, 384 (2017).
[26] L. Chen, C.-J. Huang, X.-B. Xu, Y.-C. Zhang, D.-Q. Ma, Z.-T. Lu, Z.-B. Wang, G.-J. Chen, J.-Z. Zhang, H. X. Tang, C.-H. Dong, W. Liu, G.-Y. Xiang, G.-C. Guo, and C.-L. Zou, Planar-Integrated Magneto-optical Trap, Phys. Rev. Appl. **17**, 034031 (2022).
[27] S. Kang, K. R. Moore, J. P. McGilligan, R. Mott, A. Mis, C. Roper, E. A. Donley, and J. Kitching, Magneto-optic trap using a reversible, solid-state alkali-metal source, Opt. Lett. **44**, 3002 (2019).
[28] J. P. McGilligan, K. R. Moore, S. Kang, R. Mott, A. Mis, C. Roper, E. A. Donley, and J. Kitching, Dynamic Characterization of an Alkali-Ion Battery as a Source for Laser-Cooled Atoms, Phys. Rev. Appl. **13**, 044038 (2020).
[29] J. P. McGilligan, K. R. Moore, A. Dellis, G. D. Martinez, E. de Clercq, P. F. Griffin, A. S. Arnold, E. Riis, R. Boudot, and J. Kitching, Laser cooling in a chip-scale platform, Appl. Phys. Lett. **117**, 054001 (2020).
[30] A. Strangfeld, B. Wiegand, J. Kluge, M. Schoch, and M. Krutzik, Compact plug and play optical frequency reference device based on Doppler-free spectroscopy of rubidium vapor, Opt. Express **30**, 12039 (2022).
[31] S. Madkhaly, L. Coles, C. Morley, C. Colquhoun, T. Fromhold, N. Cooper, and L. Hackermüller, Performance-Optimized Components for quantum Technologies via Additive Manufacturing, PRX Quantum **2**, 030326 (2021).
[32] S. Lecomte, E. Fretel, G. Mileti, and P. Thomann, Self-aligned extended-cavity diode laser stabilized by the Zeeman effect on the cesium D2 line, Appl. Opt. **39**, 1426 (2000).
[33] R. P. Middlemiss, A. Samarelli, D. J. Paul, J. Hough, S. Rowan, and G. D. Hammond, Measurement of the earth tides with a MEMS gravimeter, Nature **531**, 614 (2016).
[34] P. F. Griffin, K. J. Weatherill, and C. S. Adams, Fast switching of alkali atom dispensers using laser-induced heating, Rev. Sci. Instrum. **76**, 93102 (2005).
[35] E. A. Donley, T. P. Heavner, F. Levi, M. O. Tataw, and S. R. Jefferts, Double-pass acousto-optic modulator system, Rev. Sci. Instrum. **76**, 63112 (2005).
[36] S. Dyer, P. F. Griffin, A. S. Arnold, F. Mirando, D. P. Burt, E. Riis, and J. P. McGilligan, Micro-machined deep silicon atomic vapor cells, J. Appl. Phys. **132**, 134401 (2022).
[37] A. T. Dellis, V. Shah, E. A. Donley, S. Knappe, and J. Kitching, Low helium permeation cells for atomic microsystems technology, Opt. Lett. **41**, 2775 (2016).
[38] A. Bregazzi, P. F. Griffin, A. S. Arnold, D. P. Burt, G. Martinez, R. Boudot, J. Kitching, E. Riis, and J. P. McGilligan, A simple imaging solution for chip-scale laser cooling, Appl. Phys. Lett. **119**, 184002 (2021).
[39] D. A. Steck, Rubidium 87 d line data, Available Online http://steck.us/alkalidata (2001).